Analysis of time-resolved PIV measurements of a confined co-flowing jet using POD and Koopman modes

By Onofrio Semeraro, Gabriele Bellani & Fredrik Lundell

Linné Flow Centre, KTH Mechanics
SE-100 44 Stockholm, Sweden

Modal analysis by proper orthogonal decomposition (POD) and dynamic mode decomposition (DMD) of experimental data from a fully turbulent flow is presented. The flow case is a turbulent confined jet with co-flow, with Reynolds number based on the jet thickness of Re=10700. Experiments are performed with time-resolved Particle Image Velocimetry (PIV). The jet is created in a square channel with the confinement ratio is 1:5. Statistics of the flow are presented in terms of mean and fluctuating fields. Analysis of spatial spectra and temporal spectra reveal the presence of dominant wavelengths and frequencies embedded in broad-band turbulent spectrum. Frequencies in the shear layer migrate from $St \approx 1$ near the jet inlet to $St < 0.1$ at 18 jet thickness downstream.

This flow case provides an interesting and challenging benchmark for testing POD and DMD and discussing their efficacy in describing a fully turbulent case. At first, issues related to convergence and physical interpretation of the modes are discussed, then the results are analyzed and compared. POD analysis reveals the most energetic spatial structures that are related to the flapping of the jet; a low frequency peak ($St = 0.02$) is found when the associated temporal mode is analyzed. Higher order modes revealed the presence of faster oscillating shear flow modes combined to a recirculation zone near the inner jet. The flapping of the inner jet is sustained by this region. A good agreement is found between DMD and POD; however, DMD is able to rank the modes by frequencies, isolating structures associated to harmonics of the flow.

1. Introduction

While until the last decade investigations of turbulent flow fields were mainly performed based on a local approach – *e.g.* hot-wire or Laser Doppler Velocimetry (LDV) single point measurements – recent advances in experimental techniques – *e.g.* high-speed stereo and tomographic particle image velocimetry (PIV) – and direct numerical simulations (DNS) have provided access to

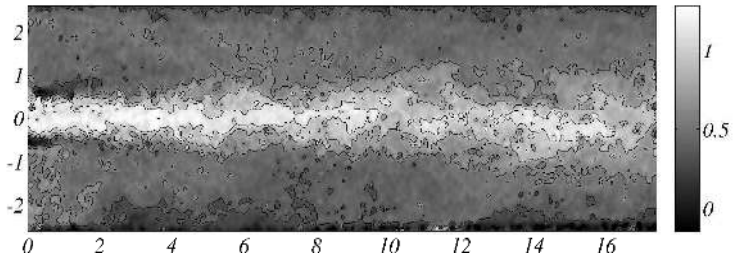

FIGURE 1. Example of PIV snapshots. The contours show the streamwise velocity component.

spatially and temporally resolved flow data. This also changed the approach to data analysis. Local analysis of temporal spectra and autocorrelations have been very useful tools to investigate coherent structures (Hussain 1986) from local time series, but with the advent of PIV and similar techniques that introduced spatially resolved data many other methods could be applied. For example one of the classical problems of the analysis of local time series is to convert from temporal to spatial scales. Very often Taylor's hypothesis of frozen turbulence is used to go from the former to the latter. Having temporally and spatially resolved data from DNS, Álamo & Jiménez (2009) uses spatio-temporal spectra and correlations to measure directly convection velocities in wall bounded turbulent flows and proposed correct Taylor's hypothesis.

However, in order to fully exploit the potential of these techniques, it is becoming increasingly important to develop tools that have a global view, which can give an insight not only on the topology of the coherent structures but also on the dynamics. This is of great importance for understanding complex natural or industrial flows, such as atmospheric and environmental flows, combustion chambers, etc. One possible approach to simultaneously make use of the temporal and spatial resolution is to use snapshots of the flow field obtained by time-resolved PIV (see figure 1) or DNS to build a matrix that somehow contains information about the dynamics of the system. Understanding what are the most relevant dynamic structures in a flow is extremely important from a physical point of view to study the instability mechanisms that lead to transition to turbulence or the coherent structures hidden in the turbulent flows, but also, from an engineering point of view, to help building reduced order models that can be used in the design and optimization of complex flow systems (Ilak & Rowley 2008; Bagheri *et al.* 2009).

1.1. *Snapshot-based modal analysis*

Among the snapshot-based methods, one of the most commonly used is the proper orthogonal decomposition (POD) (see, e.g., Holmes *et al.* 1996; Sirovich 1987). POD ranks the modes based on the most energetic structures as solution

of the eigenvalue problem related to the cross-correlation matrix computed from the snapshots. The most energetic modes often (but not necessarily) correspond to the most relevant coherent structures of the flow. The temporal information can be recovered using the bi-orthogonal decomposition (BOD), (Aubry 1991). Two sets of modes are computed, related to the two alternative ways of computing the cross-correlation matrix; indeed, the eigenvectors of the temporal-averaged cross-correlation matrix are the spatial modes, while the eigenvectors of the spatial-averaged cross-correlation matrix provide the temporal modes. Following the literature, we refer to the temporal structures as *chrono*-modes (*chronos*) and to the spatial structures as *topo*-modes (*topos*).

The spectral analysis of the *chronos* provides the temporal frequencies characterizing the *topos*, whereas the analysis in time domain can reveal the presence of temporal periodicities or limit cycles. However, a first drawback of the technique has to be mentioned here: in general, these structures are associated to more than one frequency; thus, the only possible way to rank POD modes is energy-based. Unfortunately, this criterion is not always a correct measure: low-energy structures associated to instabilities can be relevant (Noack *et al.* 2008). Moreover, this is a statistical method, hence the results obtained are intrinsically connected to the conditions in which the snapshots were obtained.

Recently, the dynamic mode decomposition (DMD) has also been applied to the analysis of experimental data and the results have been encouraging (Schmid *et al.* 2010). The DMD algorithm belongs to the category of the Arnoldi methods, widely used for the computation of the eigenvalues and related eigenvectors for linearized flow system (Ruhe 1984). In Schmid (2010), an improvement of the method is introduced and applied to nonlinear flows, also for experimental cases. From the mathematical point of view, the theoretical background relies on the spectral analysis of the Koopman operator (Mezić 2005); indeed, as shown in Rowley *et al.* (2009), the DMD algorithm approximates the Koopman modes, which can be seen as the averaged harmonic components of the flow, oscillating at certain frequencies given by the eigenvalues of the operator. From the physical point of view, it can be shown that the Koopman modes coincide with the global modes for linearized flows, and with the Fourier modes for periodic flows (see Bagheri 2010).

1.2. *Aim of the paper*

In this paper we focus on the analysis of time-resolved PIV measurements of a turbulent co-flowing jet confined in a square channel. The flow case has been chosen not only because it is relevant for several practical applications (papermaking, combustion engines, etc.) but also for its complexity, since it is a fully turbulent flow that also contains periodic structures as, for example, the flapping of the inner jet due to the interaction with recirculating areas on its sides (Maurel *et al.* 1996; Davidson 2001; Goldschmidt & Bradshaw

1973). These periodic structures can be hard to identify with spectral analysis, since they are often embedded in the turbulent flow, however here we try to identify them by means of POD and DMD. Issues concerning the choices of the snapshots and convergence are addressed and the results obtained with two methods are discussed.

1.3. *Structure of the paper*

The paper is organized as follows. In section 2, a brief theoretical overview of the modal analysis is proposed. The experimental setup is briefly described in section 3; details of the measurement technique and the flow quality are provided. Section 4 is devoted to the spectral analysis of the flow; spatial distribution of the dominant frequencies are discussed. The analysis of the coherent structure using POD is given in section 5, while the Koopman analysis is carried out in section 6. The paper ends with a summary of the main conclusions (section 7).

2. Theoretical background

The aim of this section is to provide a brief theoretical background of the modal decompositions used here. First, proper orthogonal decomposition is introduced. In the second part, Koopman modes analysis is summarized; the focus of the section is mainly on the DMD that provides an approximation of the modes; for a detailed description of the numerical methodology we refer to Schmid (2010), while more theoretical details are provided by Mezić (2005), Rowley *et al.* (2009) and Bagheri (2010).

2.1. *Proper Orthogonal Decomposition*

Proper orthogonal decomposition (POD) is a well known method for extracting coherent structures of a flow from a sequence of flow-field realizations. Given a dataset of flow realizations $\{u(t_1), u(t_2), \ldots, u(t_m)\}$ stacked at m discrete times – usually referred as snapshots or *strobes* – POD ranks the most energetic structures of the flow, computed as solution of the eigenvalue problem

$$\int_X R^* (x, x') \, \varphi_k dx' = \lambda_k \varphi_k (x) \,, \tag{1}$$

where the integral is defined on the spatial domain and

$$R^* (x, x') = \int_T u (x, t) \, u (x', t)^T dt \tag{2}$$

is the time-average cross-correlation; the integral is performed in time domain. By definition, the function R^* is positive semidefinite. The eigenfunctions $\mathbf{\Phi} = \{\varphi_1, \varphi_2, \ldots, \varphi_m\}$ are orthogonal and real-valued, while each eigenvalue λ_k contains the energy associated to each mode.

The technique was originally proposed as a statistical tool by Loève (1978); in this context, it is usually referred in literature as Karhunen-Loève decomposition (KL). According to the related theorem, a random function can be expanded as a series of deterministic functions with random coefficient. In such a way, the deterministic part – represented by the POD modes – is separated from the random part. Lumley (1970) applied the method to turbulence analysis; the flow field is expanded using the spatial eigenfunctions obtained from the KL decomposition, where the statistical ensemble employed for the decomposition is represented by a dataset of snapshots.

The temporal information can be recovered projecting back the entire sequence of snapshots on the obtained basis; the projection results in time coefficients series related to the spatial structures. An alternative way to proceed is formalized by Aubry (1991), where bi-orthogonal decomposition (BOD) is introduced. Essentially, a second eigenvalue problem related to the temporal cross-correlation function

$$R^{**}(t,t') = \int_X u(\mathbf{x},t)\, u(\mathbf{x},t')^T d\mathbf{x} \tag{3}$$

is cast. Denoting the eigenvectors obtained from the diagonalization of (3) as $\mathbf{\Psi} = \{\psi_1, \psi_2, \ldots, \psi_m\}$, it can be shown that the following correspondence between spatial and temporal modes holds

$$\psi_k = \lambda_k^{-1} X_t \varphi_k, \tag{4}$$

where $X_t : X \to T$ is a mapping between the temporal and spatial domain; this decomposition allows to split the space and the time dependence in the form

$$u(x,t) = \sum_{k=1}^{m} \lambda_k \varphi_k(x)^T \psi_k(t) \tag{5}$$

It can be shown that a projection onto the space spanned by m POD modes provides an optimal finite-dimensional representation of the initial data-set of dimension m (Holmes *et al.* 1996).

The temporal structures give access to the analysis of the frequencies dominating each modes; in general, more then a frequency is identified for each structure.

2.2. *Approximating Koopman modes: dynamic modal decomposition*

As already noticed, although frequencies are captured by the *chrono*-modes, we cannot identify structures related to only one frequency using POD. Moreover, the correlation function provides second-order statistics ranked according to the energy content; in general, low-energy structures can be relevant for a detailed flow analysis. Koopman modes analysis is a promising, novel technique that can tackle these drawbacks. The method was recently proposed by Rowley *et al.* (2009) and is also available for experimental measurements.

In order to describe this technique, we need to introduce the definition of *observable*. An observable is a function that associates a scalar to a flow field; in general, one does not have access to the full flow field in experiments: the velocity - or the other physical quantities are probed at a point, using hot wires, or in a plane, using PIV. However, considering a fully nonlinear flow, the analysis of the observable for a statistically long interval of time is sufficient to reconstruct the phase space and investigate the flow dynamics. By definition, the Koopman operator U is a linear mapping that propagates the observable $a(\mathbf{u})$

$$Ua(\mathbf{u}) = a(\mathbf{g}(\mathbf{u})) \tag{6}$$

and is associated to the nonlinear operator $\mathbf{g}$. The spectral analysis of the operator provides information on nonlinear flows; in particular, the technique allows to compute averaged harmonic components of the flow, oscillating at certain frequencies given by the eigenvalues of the operator, hereafter indicated with μ. In particular, the phase of the eigenvalue $\arg(\mu)$ determines the oscillating frequency.

The DMD algorithm proposed by Schmid (2010) provides modes that approximate the Koopman modes, as shown by Rowley *et al.* (2009) and Bagheri (2010); the complete demonstration is beyond the scope of this paper, however it is relevant to outline briefly the main steps of the DMD algorithm.

Essentially, the DMD algorithm enters the category of the Arnoldi methods for the computation of the eigenvalues and related eigenvectors. A projection of the system is performed on a basis; the best - and computationally more involved - choice is represented by an orthonormal basis. In the classical Arnoldi method the basis is computed via a Gram-Schmidt orthogonalization (Arnoldi 1951; Saad 1980), that requires a model of the system. A second possibility is given by forming the projection basis simply using a collection of samples or snapshots (Ruhe 1984). This alternative represents the most ill-conditioned among the possible choices, but can be applied in cases when a model of the system is not available.

Given a snapshot at time t_j, the successive snapshot at a later time t_{j+1} is given by

$$\mathbf{u}_{j+1} = \mathbf{A}\mathbf{u}_j \tag{7}$$

The resulting sequence of snapshots $\mathbf{X}_r = [\mathbf{u}_1 \quad \mathbf{A}\mathbf{u}_1 \quad \mathbf{A}\mathbf{u}_2 \quad \dots \quad \mathbf{A}\mathbf{u}_r]$ will become gradually ill-conditioned; indeed, the last columns of it will align along the dominant direction of the operator $\mathbf{A}$. This observation motivates the possibility to expand the last snapshot r on a basis formed by the previous $r-1$ ones, as

$$\mathbf{u}_{r+1} = c_1\mathbf{u}_1 + c_2\mathbf{u}_2 + \ldots + c_r\mathbf{u}_r + \tilde{\mathbf{u}}_{r+1}. \tag{8}$$

Here, $\tilde{\mathbf{u}}_{r+1}$ indicates the residual error. The aim is to minimize the residual such that $\tilde{\mathbf{u}}_{r+1} \perp \mathbf{X}_r$; a least square problem is cast, such that the elements c_j

are given as a solution of it. Introducing the companion matrix

$$\mathbf{M} = \begin{pmatrix} 0 & 0 & \cdots & 0 & c_1 \\ 1 & 0 & \cdots & 0 & c_2 \\ 0 & 1 & \cdots & 0 & c_3 \\ \vdots & & \ddots & & \vdots \\ 0 & 0 & \cdots & 1 & c_r \end{pmatrix} \tag{9}$$

equation (8) is re-written in matrix-form as

$$\mathbf{A}\mathbf{X}_r = \mathbf{X}_r\mathbf{M} + \tilde{\mathbf{u}}_{r+1}\mathbf{e}_r^T. \tag{10}$$

The action of the companion matrix is clear: it propagates one step forward in time the entire sequence of snapshots, whereas the last snapshot is reconstructed using the coefficients c_j. Moreover, the equivalence represented by (8) shows that the operator $\mathbf{A} \in \mathbb{R}^n$ is now substituted by $\mathbf{M} \in \mathbb{R}^r$, with $r \ll n$. It results that the eigenvalues of $\mathbf{M}$ – usually referred as Ritz values – approximate the eigenvalues of the real system. The related eigenvectors are given by $\tilde{\mathbf{\Phi}} = \mathbf{X}_r\mathbf{T}$, where $\mathbf{T}$ are the eigenvectors of the companion matrix $\mathbf{M}$. As observed by Schmid (2010), this algorithm can be used to extract Ritz values and the related vectors from experimental data or sequence of snapshots of nonlinear simulations.

It is worth mentioning two features of the algorithm: first, the modes are characterized by a magnitude that can be easily computed as the norm of the modes $|\tilde{\phi_j}|$. The resulting amplitudes are essential for separating the wheat from the chaff: as shown by Rowley *et al.* (2009), high-amplitude modes are related to the most important and convergent eigenvectors. Moreover, (10) allows to estimate the norm of the residual error as $\|\tilde{\mathbf{u}}\| = \|\mathbf{A}\mathbf{X}_r - \mathbf{X}_r\mathbf{M}\|$. The analysis of the residuals is helpful for the identification of the snapshots dataset; indeed, the selection of Δt_s and the proper time windows of investigation are related to the residual analysis.

The linear dependency of the dataset, necessary for identifying the last snapshot, makes this method prone to convergence issues and ill-conditioness. An improvement is proposed by Schmid (2010), where a self-similar transformation of the companion matrix $\mathbf{M}$ is obtained as a result of the projection of the dataset on the subspace spanned by the POD generated from it. To this aim, a preliminary singular value decomposition (SVD) of $\mathbf{X}_r$ is performed; the SVD allows to disregard the redundant states and the transformed companion matrix is now a $full$ matrix: both these features make the eigenvalues problem better conditioned.

3. Experimental setup

The experiments are performed in a square channel whose dimension D is 50 mm. The first 300 mm of this square channel are divided into three sections of dimensions 19, 10 and 19 mm by means of two horizontal walls that span

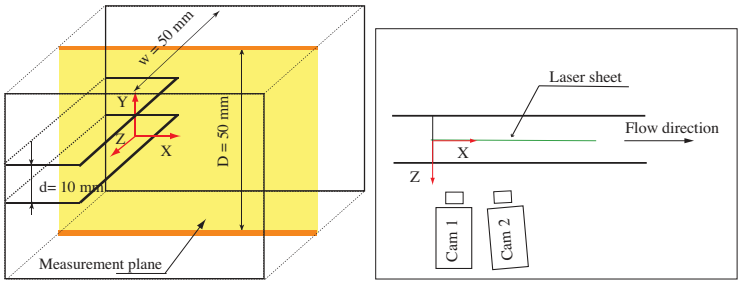

(a) Geometry and coordinate system (b) Light sheet and cameras arrangement

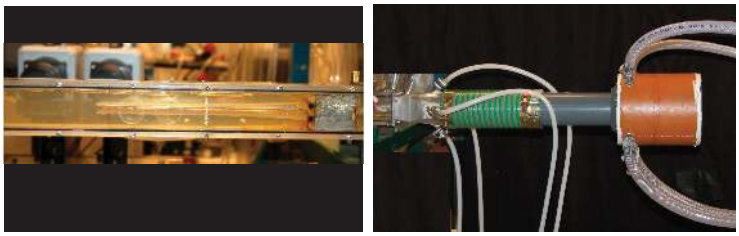

(c) Test section (d) Flow distributor

FIGURE 2. Experimental setup.

the entire width, see figure 2*c*. The end of the splitter walls corresponds to the beginning of a planar co-flowing jet, which is our measurement domain, see figure 2*a*. The thickness d of the inner jet is 10 mm, which gives a confinement ratio d/D of 1:5. The flow in the three jets is supplied by two independent pumps through two radial distributors, one connected to the inner and one to the two outer channels, see figure 2*d*. This configuration allows to control the flow rates of the inner and the outer sections independently, therefore two non-dimensional parameters can be varied in the present setup: the velocity ratio $\lambda_r = U_j/U_s$, where U_j and U_s are the centerline velocities of the inner and the outer jets respectively, and the Reynolds number $\mathrm{Re} = U_j d/\nu$, where ν is the kinematic viscosity of the fluid.
In this work we show results for $\lambda_r = 2.1$ and $Re = 10700$.

3.1. *Measurement technique*

The time-resolved measurements of the flow were done by high-speed Particle Image Velocimetry. The PIV system used in this work consists of a double cavity 10 mJ Nd:YLF laser (repetition rate 2-20000 Hz) as a light source, and two high-speed cameras (up to 3000 fps at full resolution) with resolution of 1024×1024 pixels.

The arrangement of the cameras and the laser-sheet is shown in figure 2*b*. The two cameras were used to acquire two 2-D velocity fields, each of them of 50x100 mm^2. The second camera was tilted by 5° in order to reach an overlap between the two fields of about 20 mm, so that the total downstream length over which the measurement extends is of about 180 mm.
The two cameras were calibrated by taking images of a calibration plate with known reference points *in situ*, and the calibration parameters were extracted using a pinhole-based model (see Willert 2006).
The flow was seeded with 10μm silver-coated tracer particles, and a series of double-frame, single-exposure images were acquired at a rate of 1500Hz for a total time of 4 seconds. The velocity fields were calculated using the commercial PIV software *DaVis 7.2* from *LaVision GmbH*. The algorithm used is a multi-pass correlation with continuous windows deformation and shift, which allowed to achieve a final interrogation window size of 8x8 pixels. The size of the interrogation window is of about 0.75x0.75 mm^2 in physical space, which sets the lower limit for the spatial resolution. The window overlap was 50%. For detailed information about the performance of the PIV algorithm, see Stanislas *et al.* (2008).

3.2. *Flow quality*

In order to establish the characteristics of the flow in the channel, we measured cross-stream profiles at 5 spanwise stations including the channel centerline, and spanwise profiles at the centerline of the three jets. In this paper we refer to the direction parallel to the x-coordinate as the streamwise direction, the direction parallel to y as the cross-stream and the one parallel to z as the spanwise direction. The streamwise and cross-stream velocity components are U and V, respectively.
Figure 3 shows the streamwise development of the time average of U ($\langle U \rangle$) and the root mean square ($r.m.s$) of the streamwise turbulent fluctuations u' ($\langle u'^2 \rangle$) at the channel centerline ($z = 0$). The profiles are scaled to fit the figure, and the x and y coordinates are normalized by the inner jet thickness d. Two main features can be observed in the mean velocity profiles: the boundary layers developing at the channel walls and the two wakes generated by the blunt end of the splitter walls on the profiles near the inlet. The $r.m.s.$ profiles show the characteristic local maxima at the two shear layers. The dashed lines show the centerlines of the three jet regions. The dashed-dotted lines follow the development of the jet half width L, defined as the point where $(U - U_s)/(U_j - U_s) = 0.5$.

The spanwise evolution of the velocity profiles have also been investigated to assess to what extent the flow can be considered two-dimensional. Figures 4*a* and *b* show the cross-stream profiles of $\langle U \rangle$ at 5 spanwise stations ($Z/d = -2, -1, 0, 1, 2$), whereas figures 5$a - b$ show the spanwise profiles. The latter

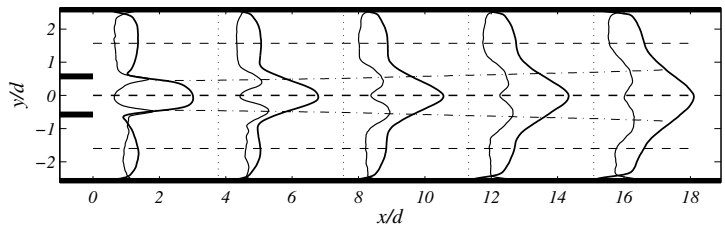

FIGURE 3. Streamwise evolution of the mean (thick line) and *r.m.s.* (thin line) profiles of U are at the channel centerline (z/d=0). The profiles are scaled to fit the figure.

has been measured by rotating the channel 90° around the x-axis, so that the light sheet was parallel to the z-axis.

These figures show that although the inlet profiles are not perfectly *top-hat*, the flow rates on upper and lower channel are quite the same and the boundary layer at the side walls never reaches the center of the channel. Therefore we can consider the flow as *quasi*-2D.

Normalized mean, *r.m.s.* and Reynolds stress profiles profiles are shown in figure 6. The normalizing scales are the local velocity excess $U_0 = U_j - U_s$ for the mean velocity, and the jet half width L for the y coordinate. From figure 6*a* we can see that the mean velocity profiles are still affected by the wake behind the walls splitter but self-similarity is reached already at $x/d = 5$, see figure 6*b*. From these figures we can also see the growth of the boundary layers from the channel walls, which however do not reach the self-similar region at the core of the jet. Figures 6*f* and 6*d* show that *r.m.s* and Reynolds stresses reach self-similarity later than the mean flow, at around $x/d = 10$, as reported by Chua & Lua (1998) in a similar flow case. It is interesting to note that the typical saddle shape of the *r.m.s* profiles is not symmetric and seem to be inclined so that the *r.m.s* values on the lower part of the channel are higher than in the upper part. This might be an indication of a recirculation zone induced by the confinement due to a slight asymmetry of the experimental setup. Recirculation zones around a jet due to confinement has been observed by Maurel *et al.* (1996); Davidson (2001); Goldschmidt & Bradshaw (1973). In these works it has been shown that the re-circulation zone can induce self-sustained oscillation of the jet. The frequency of the oscillations are dependent on the geometry and the confinement ratio but in general they have low frequency and are characterized by Strouhal numbers based on the jet thickness of $St \approx 0.01$.

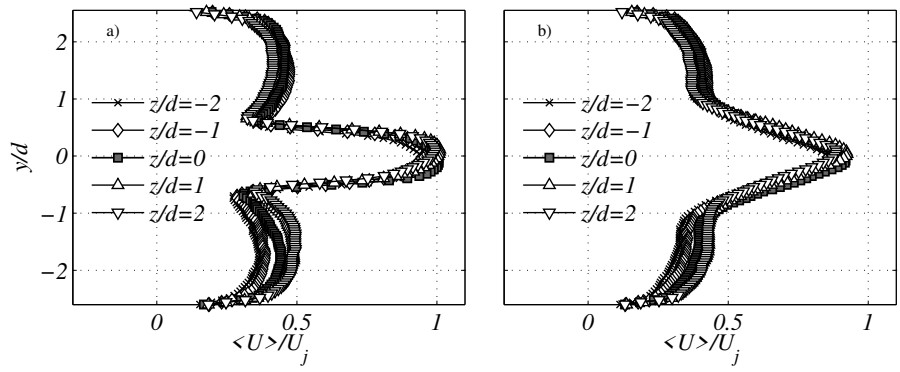

FIGURE 4. Cross-stream profiles at $x/d = 0$ (a) and $x/d = 7.5$ (b)

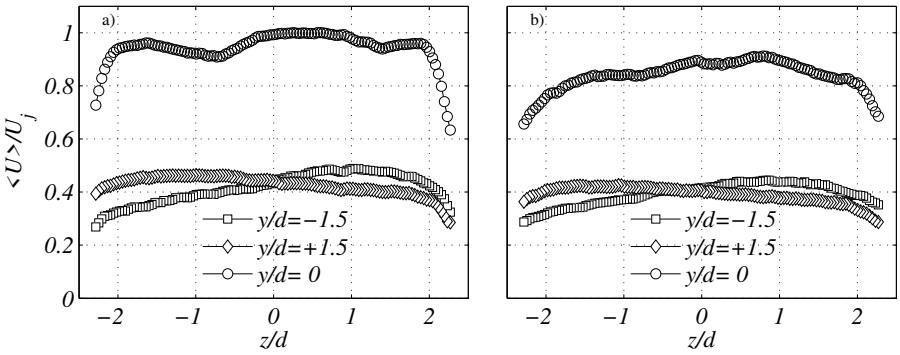

FIGURE 5. Spanwise profiles at $x/d = 0$ (a) and $x/d = 7.5$ (b)

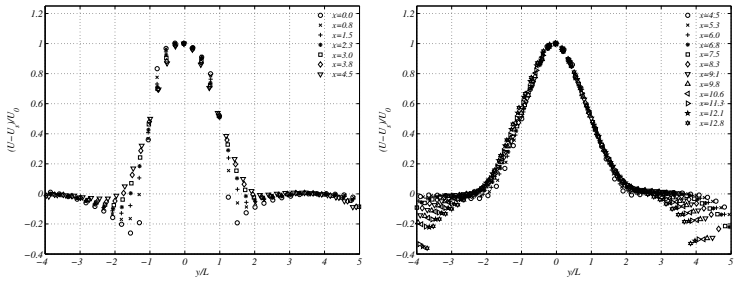

(a) $x/d < 5$ (b) $x/d > 5$

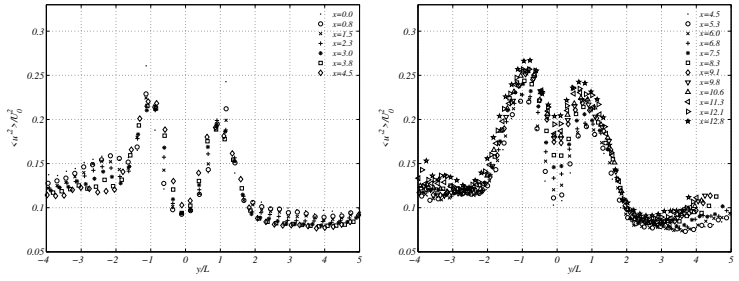

(c) $x/d < 5$ (d) $x/d > 5$

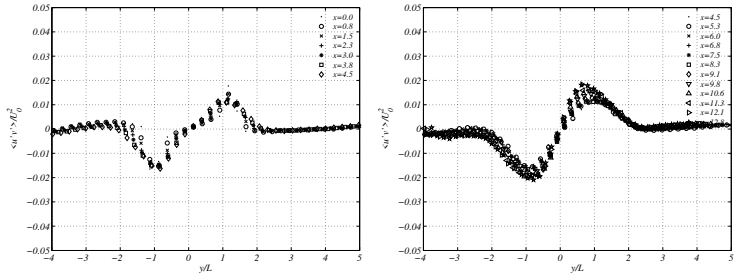

(e) $x/d < 5$ (f) $x/d > 5$

FIGURE 6. Self similar profiles of mean streamwise velocity, normal and shear stresses $\langle u' \rangle$ and $\langle u'v' \rangle$.

4. Spectral analysis

4.1. *Computational procedure*

Time resolved PIV measurements were done at the center of the channel, on the x-y plane (see figure 2). As an output of the PIV measurements, for each point of the measurement domain ($0 < x/d < 18$) we obtained a time signal made of 6000 samples for a total sampling time of 4 seconds. We therefore have spatially and temporally resolved data from which we can detect the presence of dominant wavelength and frequencies by the analysis of the Power Spectral Density (PSD). Temporal spectra are calculated using the Welch method seeking a compromise between smoothness and good resolution of the low frequencies. For the spatial spectra we followed a similar approach, but in this case the maximum length of the signal was determined by the physical length of the measurement domain, and the final PSD estimate was obtained by averaging the spectra at different time steps.

Examples of temporal and spatial spectra (Φ_u and Θ_u, respectively) can be seen in figure 7. Figure 7a shows the normalized PSD of the streamwise velocity fluctuations at 5 streamwise stations ($x/d = 0, 1.5, 7, 10, 15$) along the jet centerline. It can be seen that the slope of the spectra approaches the value of -5/3 as we move downstream, where we expect to have nearly isotropic turbulence in the jet core. Peaks might also be present in some regions of the spectra but it is hard to distinguish it from the noise, since the time series are relatively short due to the limited capabilities of PIV to acquire long time series do not allow us further smoothing.

Therefore, in order to get an idea of the dominant scales in the different regions of the flow we can plot the contours of the spectra as a function of y as shown in figure 8. The normalized spectra here are presented on a logarithmic scale, thus they are premultiplied by the frequency or wavelength vector. Figure 7(a) shows the temporal spectra computed at the jet outlet, whereas figure 7(b) shows the distribution of spatial spectra. In the latter, it can be seen that much of the energy is contained in the two regions corresponding to the shear layer, with a maximum peak located at $d/\lambda_x \approx 0.3 - 0.4$, which corresponds to about half of the channel width $D/2$ in physical terms. In the same region we can observe two peaks in the temporal spectra at $St = 1$, where St indicates the Strouhal number and is defined as $St = \frac{f(d/2)}{U_j - U_s}$, with f being the dimensional frequencies. In the rest of the domain instead, most of the energy is contained at low St, in particular in the co-flow region peaks appear at $St < 0.1$. This is another evidence of low-frequency structures, like a re-circulation zone due to the jet confinement, even if the St is higher than the one reported in previous studies. This can be explained by the fact that due to the limited length of the time series and the windowing used to compute the spectra, the resolution of the low frequencies is poor.

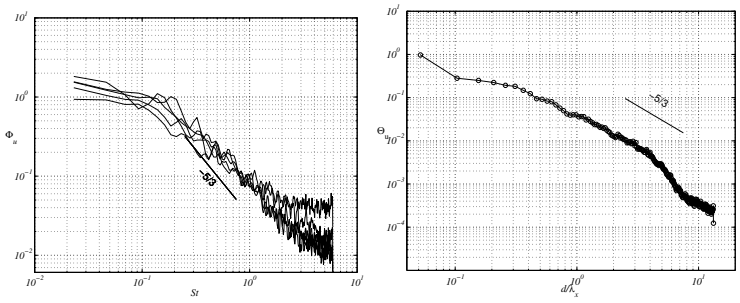

(a) $y = 0$ (b) $y = 0$

FIGURE 7. Φ_u and Θ_u at $y = 0$

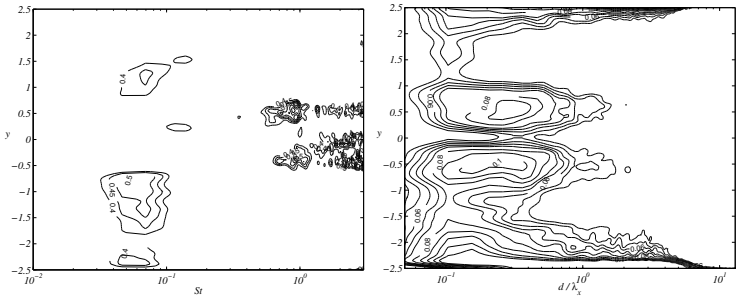

(a) $x/d = 0$ (b) $x/d = 0$

FIGURE 8. Φ_u and Θ_u at $x/d = 0$

4.2. *Spatial distribution of dominant frequencies*

The spectra shown in figure 7*a* are computed at the jet outlet. However it is interesting to analyze what happens further downstream. This is shown in figure 9, where the y distribution of Φ_u is show at 8 streamwise stations: $x/d = 0.38, 0.75, 1.13, 1.50, 3.40, 7.16, 10.90$ and 15.80. What it can be observed from this sequence is that the two high-frequency peaks in the shear layer tend to "migrate" towards lower frequencies as we move downstream, to approach the value of $St = 0.1$ for $x/d > 10$, *i.e.* in the self-similar region. This can be explained by the fact that in the region $x/d < 5$ we still have small scale/high-frequency structures due to the wake behind the splitter walls, which can influence the dynamics of the shear layer, as reported in Örlu *et al.* (2008). However, further downstream the most dominant structures are large/low frequency due to the flapping of the inner jet (Maurel *et al.* 1996; Davidson 2001; Goldschmidt & Bradshaw 1973).

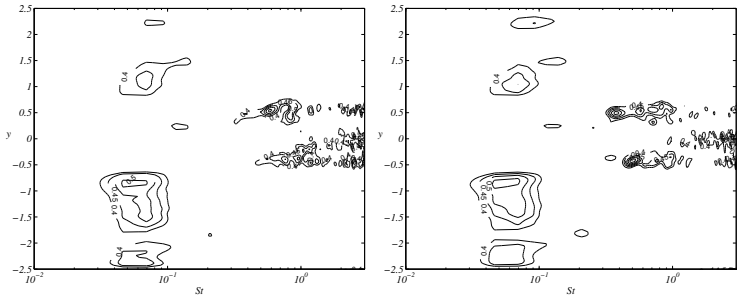

(a) $x/d = 0.38$ (b) $x/d = 0.75$

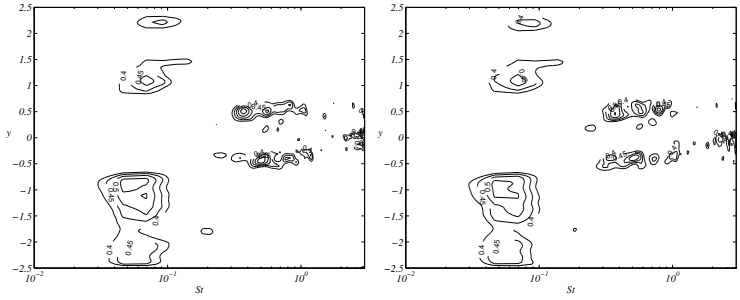

(c) $x/d = 1.13$ (d) $x/d = 1.50$

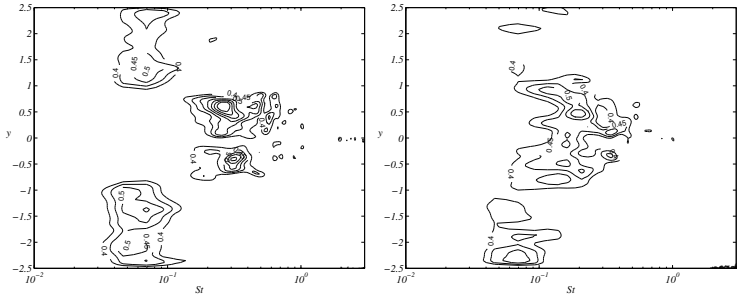

(e) $x/d = 3.40$ (f) $x/d = 7.16$

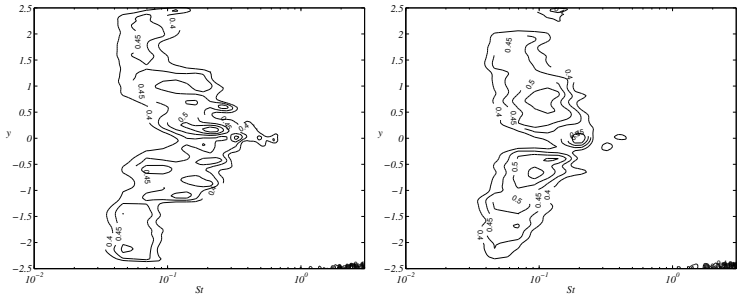

(g) $x/d = 10.9$ (h) $x/d = 15.8$

FIGURE 9. Contours of premultiplied spectra $St\Phi_u$. The contour lines are drawn at: 0.4, 0.45, 0.50, 0.55, 0.60, 0.65, 0.70.

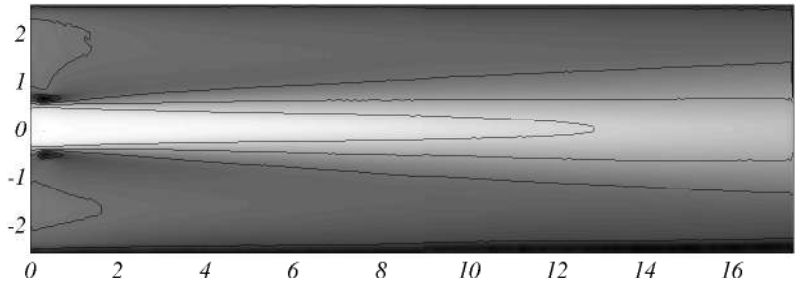

FIGURE 10. U-component of the first *topo*-modes (mean-flow).

5. Analysis of coherent structures I: POD

5.1. *Choice of the snapshots*

The mapping X_t provides a relation between the space and time domains; thus, the diagonalization of (3) provides temporal modes, while the spatial modes can be evaluated using (4). A discrete form of this procedure was introduced by Sirovich (1987). Here the author shows that the corresponding discrete form of the operator X_t can be built by stacking N_t snapshots of the flow field to form a matrix of dimensions $n \times N_t$, where n is the number of grid points in space and N_t is the number of snapshots. Therefore this method is known as *snapshot method*. The advantages of the technique relies on the dimensions of the eigenvalue problems associated with the two alternative cross-correlations; indeed, the number of snapshots stacked in time is usually smaller than the number of spatial degrees of freedom; thus, the eigenvalue problem associated with the spatial cross-correlation matrix is more expensive than diagonalizing the temporal cross-correlation; however, relation (4) provides a means for recovering the spatial modes from the temporal modes using the mapping X_t. Note that the same results can be achieved performing a singular value decomposition (SVD); in this case, the temporal structures and the spatial structures are obtained simultaneously, see Schmid (2010). The two procedures are equivalent, and the former method was used in our calculations.

When choosing the snapshots, there are two important choices to be made: the total number of snapshots N_t and the time interval between two consecutive snapshots Δt_s. In fact, as already mentioned, the modes obtained by POD are always the optimal (in a least square sense) representation of the snapshots used to compute the cross-correlation matrix, but it has to be kept in mind that POD modes are representative of the flow just as much as the cross-correlation matrix is. Therefore if we want to extract physically relevant information of the flow structures, N_t has to be chosen so that there are a sufficient number of independent samples to ensure converged statistics, and

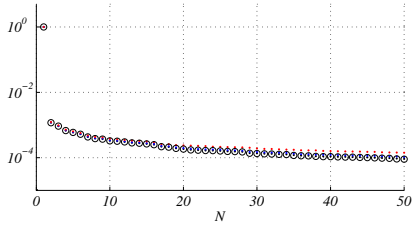

(a) Distribution of λ_k

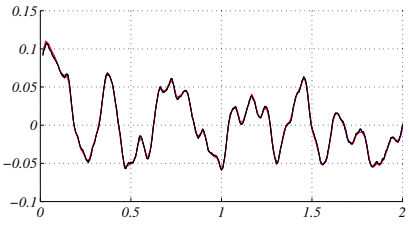

(b) *Chrono*-mode n=1

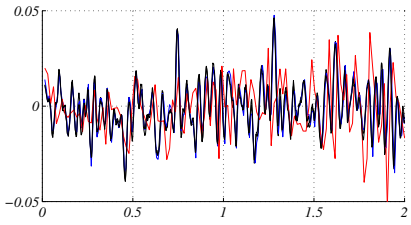

(c) *Chrono*-mode n=29

FIGURE 11. Eigenvalues and temporal modes for $\Delta_t = 1/750$ (black), 1/250 (blue) and 1/125 (red).

that the time spanned by the snapshots is long enough to contain the slowest scales of the flow. Provided the above conditions, the *topos*-mode (*i.e.* the spatial modes) do not seem to depend at all on the time of sampling Δt_s. However, when recovering the temporal information by (4), it is clear that this parameter determines the temporal resolution of the *chronos*-modes; thus, if Δt_s is too large, the *chronos*-modes associated with high frequencies do not converge. An example of this idea is shown in figures 11b and 11c, where we see the *chronos*-modes corresponding to mode number 1 and 29 respectively. It can be seen that the time series of mode 1, which shows mainly low-frequency quasi-periodic fluctuations is well captured for every Δt_s, whereas for mode 29 the time series obtained with the largest Δt_s does not follow the ones obtained with smaller time interval between the snapshots. Differences appear also in the eigenvalues, see figure 11a. The spectra obtained with Δt_s=1/750 and 1/250 are basically the same, whereas the spectrum computed with the largest interval diverges as the number of modes, N, increases.

5.2. *Spatial and temporal modes*

From the first convergence analysis of the previous section we conclude that a Δt_s of 1/250 is adequate to temporally resolve the structures of our flow case.An acquisition time of 3.3s is chosen, corresponding to $N_t = 834$ is fixed which is on the order of about three times the slowest time scale of the flow.

As a convergence test, we take three sets of 5000 snapshots which differ from a time offset of ≈ 0.2s from each other. The convergence is directly analyzed by comparing the POD eigenvalues obtained from each set. A relative error of order $O(10^{-4})$ is obtained among the set; this value is deemed sufficient to guarantee convergence of the results. A further numerical test is related to the orthogonality of the modes. The condition is satisfied down to $O\left(10^{-13}\right)$ for all the modes.

In figure 11a, the eigenvalues related to the POD modes are shown; the portrait obtained is rather typical: the first mode contains 97% and is related to the meanflow of the jet. Hereafter, we will denote it as 0-mode. As expected, the corresponding *chrono*-mode is constant.

The remaining modes are related to the fluctuating part of the flow field, and the sum of their eigenvalues represents the turbulent kinetic energy (TKE). A first eye-inspection of the *topo*-modes reveals that some of the modes come in pairs. This is evident for example for mode 1 and 2, as shown in figures 12a-b. Here we can see that the structure of the two modes is the same, except for a shift in phase: they are both anti-symmetric with respect to the x-axis, and they both present two large lobes located downstream. The analysis of the corresponding *chrono*-modes confirms the similarities between the two structures: they both show periodicity with similar amplitude of the peaks. This is an evidence that the modes represent a wave-like periodic structure of the flow. In fact, since the POD modes are real, two modes are needed to describe a flow structure traveling as a wave (see e.g. Rempfer & Fasel 1994). From a physical point of view this structure represent the flapping of the jet, which is the most energetic feature of the flow. A frequency analysis of the signal from the *chrono*-modes (see figure 12d) shows that there is a very clear peak at $St = 0.02$ for both mode 1 and 2. This is in line with the previous frequency measurements of flapping of confined turbulent jets mentioned in the earlier sections. It is remarkable that, although in general each POD mode can be associated with more than one frequency, the peak at $St = 0.02$ appears more clearly than in the spectral analysis of the time series. This is because the time series contains information about all the turbulent structures, whereas the considered modes isolate only one feature.

Finally, figure 12e shows the temporal orbit obtained by projecting the flow field onto the subspace spanned by φ_1 and φ_2. It is clear that the trajectory shows an attractor-like behavior, similar to what we would observe from the vortex shedding behind a cylinder. This confirms the impression that the modes represent a physical coherent structure and are important for the reconstruction of the dynamics of the flow system.

In figure 13a-c, the modes 3-5 are shown. These modes are characterized by smaller scales and higher frequencies (see figures 13d and 13e) than the previous

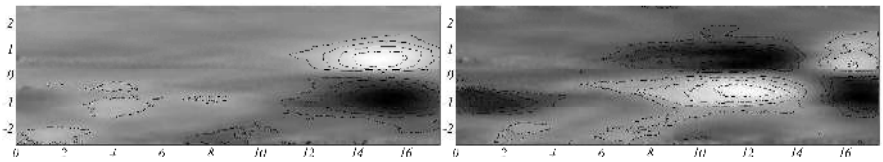

(a) First *topo*-mode (b) Second *topo*-mode

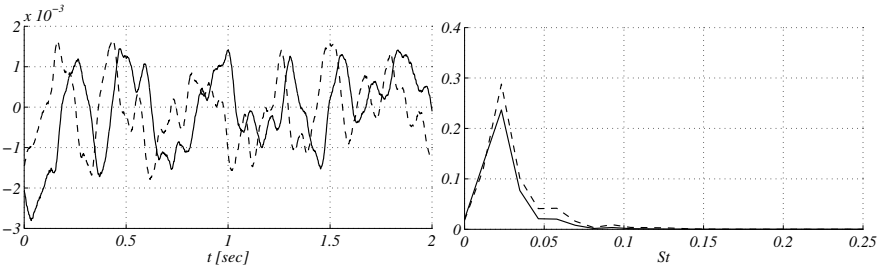

(c) *Chrono*-modes: time domain (d) *Chrono*-modes: frequency domain

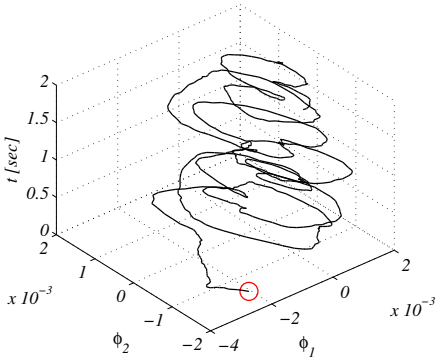

(e) Temporal orbit in the subspace spanned by φ_1 and φ_2

FIGURE 12. The first and second POD modes are analysed. The streamwise component of the *topo*-modes is shown. The first *chrono*-mode is indicated with a solid line, the second one with a dashed line.

ones, but they are also clearly associated with oscillations of the shear layer. One interesting feature emerging from these modes is a structure in the lower part of the channel that seems to be associated with a recirculation zone. This recirculation might be responsible for the jet self-sustained oscillations, which is confirmed by the fact that in the POD this feature appears in the mode

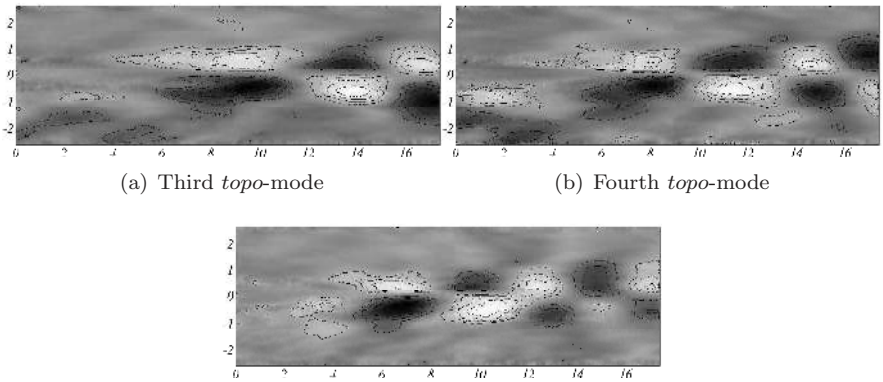

(a) Third *topo*-mode (b) Fourth *topo*-mode

(c) Fifth *topo*-mode

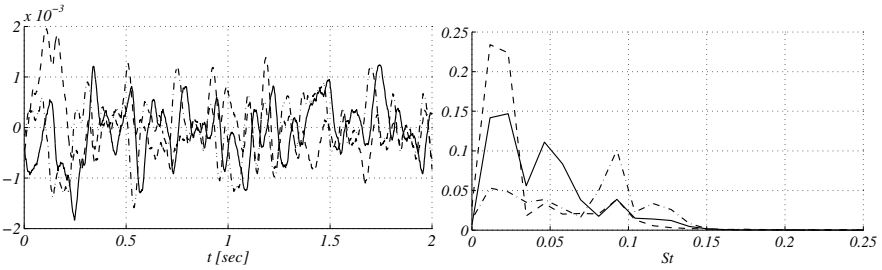

(d) *Chrono*-modes: time domain (e) *Chrono*-modes: frequency domain

FIGURE 13. The third, fourth and fifth POD modes are shown. The streamwise component of the *topo*-modes is shown. The first *chrono*-mode is indicated with a solid line, the second one with a dashed line and the third with a dashed-dotted line.

corresponding to shear layer oscillations. The analysis of the related *chrono*-modes in spectral space (figure 13e) reveals the presence of three well defined frequencies in all these modes; however, the peaks have different magnitudes in the three modes.

Note that the frequency increases as the energy associated to the modes decreases. This might be a consequence of the fact that lower energy is associated to smaller scales; indeed, an eye-inspection of the modes shows that, as the rank increases, the *topo*-modes are characterized by low-energy structures, progressively smaller, while the corresponding *chrono*-modes are dominated by higher frequencies. This trend is confirmed by figure 14, where the normalized spectrum for each of the first $N = 100$ modes is depicted. In addition, it can be noticed that strong peaks occur for high-energy modes; moreover the

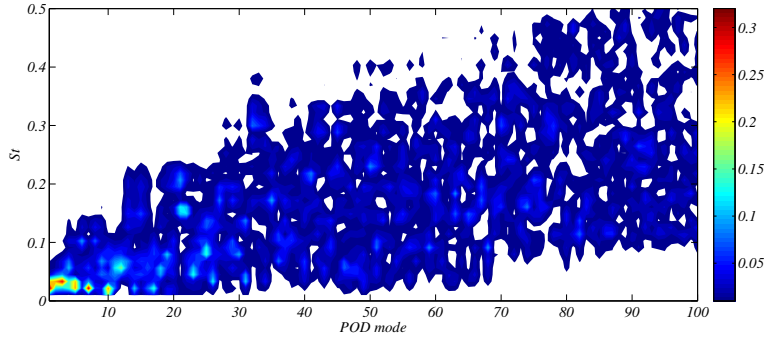

FIGURE 14. Spectral analysis of the first $N_m = 100$ *chrono*-modes.

number of peaks increase with the order of the modes; thus, modes containing high-energy, are also characterized by few and well distinguished frequencies (*i.e.* they are associated with periodic coherent structures).

6. Analysis of coherent structures II: Koopman modes

6.1. *Convergence tests and selection of the modes*

As mentioned in section 2.2, the linear dependency of the snapshots dataset allows to write (10); however, this feature makes the method prone to ill-conditioness. Thus, to ensure the effectiveness of the numerical procedure, we carry out $ad - hoc$ tests. In particular, the choice of an adequate sample of snapshots turns out to be crucial; following the guidelines already discussed for the POD, we select as parameters for the choice, the number of snapshots N_t and the sampling time Δt_s, *i.e.* the interval between two successive snapshots. To this aim, we make use of the residuals $\tilde{\mathbf{u}}$ (see section 2.2), analysing their trend when changing N_t or Δt_s: the main idea is to select the set of parameters that guarantees the smaller residual.

Figure 15a reports the behavior of the residual as function of time. Two different sampling-strides are considered: the dashed line indicates a stride $N_s = 20$, while for the continuous line $N_s = 10$. The overall trend shows a reduction of the residual value as the number of samples increases. In figure 15(b), the residual value is analysed as function of the number of snapshots spanning the sampling interval Δt_s for two datasets: the original PIV measurements (dashed lines) and a filtered set of snapshots (solid lines). The cut-off frequency of the filter is of 250 Hz, which reduces the measurement noise but leaves unaltered all the relevant scales of the flow. The third parameter considered in the graph is the time-window of observation: the lines are darkened progressively according to the chosen final time of the time-window, from $t = 0.667$ to 4.0. We can summarize as follows the main results included

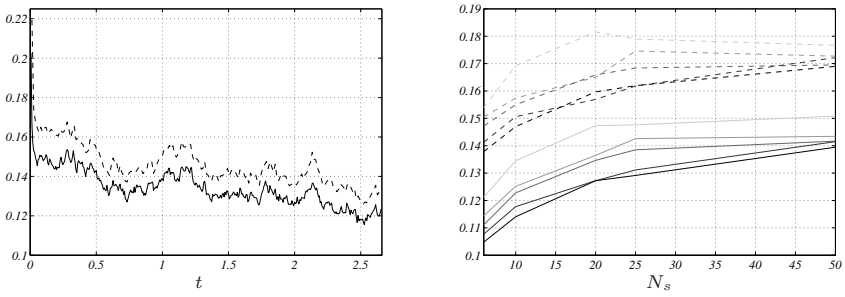

(a) Residuals vs time (b) Residuals vs sampling-stride

FIGURE 15. Residual analysis - in (a) the dashed line indicates the residuals associated to the original data, while the solid line indicates the filtered data (250Hz). In (b) the same legend is adopted; darker lines are related to longer time windows of sampling.

in figure 15(b):

1. In all cases, a monotonic reduction of the value is obtained when reducing Δt_s.
2. Longer windows of observation yields better results.
3. Fixing the sampling parameters and using the filtered data, an improvement of about 20% is observed for the residual values.

However, we need to keep in mind also the physical point of view; clearly, longer sampling intervals act as a filter; thus, high-frequency modes cannot be resolved if a too large Δt_s is chosen. The filtering of the dataset theoretically imposes the lower limit $\Delta t_S = 1/250$; however, the SVD pre-processing of the dataset allows to circumvent the problem, disregarding the states numerically not relevant, usually related to linear dependencies. In more detail, denoting with σ the singular values computed for the snapshots dataset, the ratio σ_j/σ_1 provides an estimation of the condition number. A threshold can be selected: as a rule of thumb, one can consider the numerical precision – if DNS data are used – or the precision given by the experimental instrumentation. The states associated to the singular values that are below this threshold can be disregarded.

The amplitudes associated to the Koopman modes serve efficiently as parameter for the selection of the modes. Here a further convergence criterion is introduced due to the complexity of the analysed flow. In particular, three sets

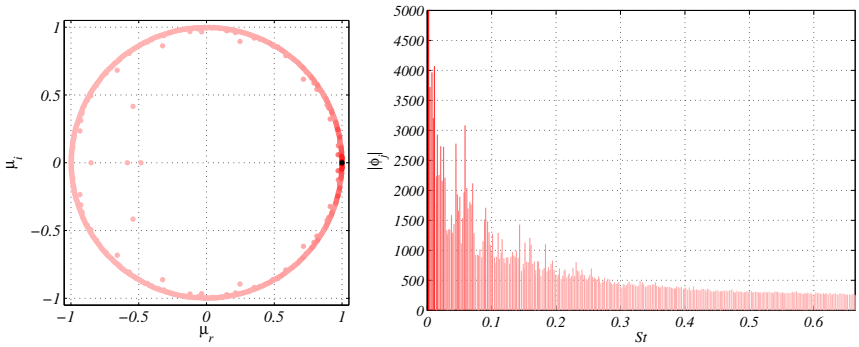

(a) Discrete spectrum (μ)

(b) Amplitudes associated to St

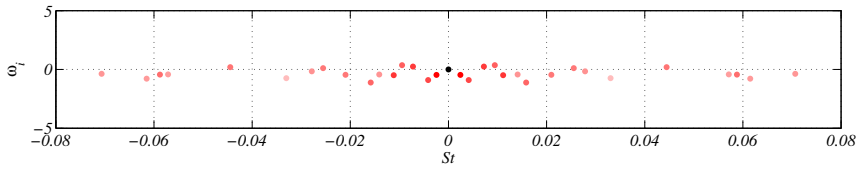

(c) Continous spectrum (ω) after the selection. The real frequency is reported as St.

FIGURE 16. The spectrum obtained from the DMD is shown in (a). In (b) the associated amplitudes are shown (except for the first mode). The physical relevant ones are kept in (c).

of snapshots are formed: each of them is characterized by $N_t = 700$ and a snapshots stride of $\Delta N_t = 8$: the resulting interval in time for each case is $\Delta t = 3.3$s; the sets differ in the selected time-window, which slides forward with a small Δt. Since the investigation involves a flow fully developed after the transient, we expect that the most important features appear in all the considered sets: thus, our procedure relies on the comparison of the modes obtained applying the DMD to the three sets. We consider convergent the eigenvalues that for each set had a difference in frequency below a chosen tolerance. Moreover, the corresponding eigenvectors are compared via a cross-correlation, in order to ensure the physical correspondence among the modes picked in each set.

6.2. *Spatial modes by DMD*

In figures 16a, the discrete spectrum obtained for the first set – spanning the time interval $t = [0, 3.3s]$ – is shown. As observed in Mezić (2005) and Bagheri (2010), for $t \to \infty$, the Koopman operator is unitary, thus all the eigenvalues will lie exactly on the unit circle. Indeed, we can observe that nearly all the eigenvalues lie close to the unit circle. The amplitudes of the modes are depicted in 16b with the same color; the darker the color, the higher the amplitude of

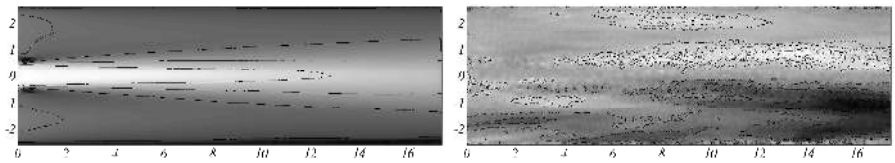

(a) Mean flow (b) $St < 0.01$

FIGURE 17. The streamwise component of the meanflow is shown in (a). In (b) the low frequency mode associated with the highest amplitude is shown.

the mode. The peaks are still quite numerous and, although quite well resolved, the result demonstrates the necessity of introducing the convergence method for the selection of the modes physically meaningful.

After the selection is performed, only a part of the eigenvalues is kept, as shown in figure 16c where the corresponding Strouhal number is reported for each of them; in the latter figure, the spectrum is in continuous form, obtained using the relation $\omega = \log \mu/(\Delta t_s)$. In particular, the selected modes approach the 0 growth limit; indeed, in a nonlinear flow we cannot expect growing/decaying structures. The presence of a growth rate is mainly related to the time-window of observation; in principle, due to the property of the Koopman operator referred above, infinite time of observation would lead to eigenvalues characterized by null growth. The distance from the $\omega_i = 0$ can be also regarded as a convergence test: the more the eigenvalues are close, the more are convergent the modes, *i.e.* physically relevant.

The black dot indicates the mean-flow, appearing as the 0 frequency mode in the continuous spectrum and shown in figure 17a. The first mode is characterized by a low Sthroual number (figure 17b; the structures are anti-symmetrical with the respect to the streamwise direction and mostly located downstream, where two elongated lobes dominate the structures. This mode, and the ones characterized by low frequency, closely resemble the POD modes shown in figure 12; indeed, from a physical point of view, these structure are related to the flapping of the jet, as confirmed by the St in line with the previous frequency measurements.

The DMD/Koopman mode analysis turns out particular fruitful for the analysis of the recirculation close to the jet-inlet. In figure 18a, the mode related to this feature is shown; an elongated lobe is observed in the lower, upstream region of the domain where the previous analysis showed the presence of recirculation. The corresponding St number is in agreement with the former measurements. Note that this region was highlighted also by POD analysis; however, the modes (figure 13) were characterized by the simultaneous presence

of the shear flow and the recirculation phenomena, as confirmed by the analysis of the *chrono*-modes (figure 13d-e). Using the Koopman modes, it is now possible to clearly distinguish the physical phenomena related to the frequency peaks (figure 13e). In particular, figures 18b-d show the shear-flow structures associated to the Strouhal number obtained by spectral analysis (13e). The modes are anti-symmetric; the finer structures located downstream in the domain are associated to higher frequencies and closely resemble the structure already observed with the POD analysis.

7. Conclusions

POD and DMD have been applied to experimental data from PIV measurements of a turbulent confined jet with co-flow. The jet is fully turbulent, however the results from the spectral analysis have shown the presence of periodic features, arising from the flapping of the jet induced by a recirculation zone on the side of the inner jet.

Jet flapping appears as two large structures located downstream ($x/d > 10$) on the first two POD modes. These two modes appear to be coupled to each other, since they only differ from each other by a phase shift both in time (from the analysis of the *chrono*-modes) and in space. Frequency analysis of the *topo*-modes show a clear peak at $St = 0.02$, which is in line with previous experimental results. Modes 3, 4 and 5 show the coupling between the recirculation zone near the inlet and shear-layer oscillation, which is believed to be the leading sustaining mechanism for the jet flapping. Although the recirculation zone and the shear layer oscillations are characterized by different frequencies, they appear coupled in the POD modes since the two structures are correlated. Instead, in the DMD modes the two structures appear in two separate modes; thus, the method efficiently isolates structures with a single frequency. The peaks found by spectral analysis of the *topo*-modes are in good agreement with the frequencies found by DMD.

DMD modes are selected with an iterative procedure that identify *consistent* modes by projecting the results of one iteration on the previous one obtained with another set of snapshots that have an offset origin in time, and retaining those whose projection is larger than a user defined threshold. We observed that the most consistent modes (*i.e.* those who *survive* increasing the threshold) are those whose growth rate is closer to 0; moreover, these modes are generally the ones characterized by high amplitude, in accordance with the theoretical results.

Gabriele Bellani and Fredrik Lundell thank the Swedish energy agency for fundings. Computer time was provided by SNIC (Swedish National Infrastructure for Computing). Prof. Hiroshi Higuchi is acknowledged for helping in the design and development of the experimental setup. Dr. Shervin Bagheri and Johan Malm are acknowledged for fruitful discussions.

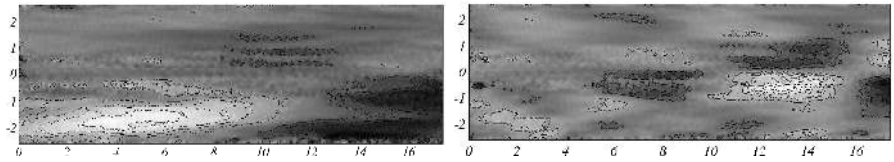

(a) $St = 0.01$ (b) $St = 0.04$

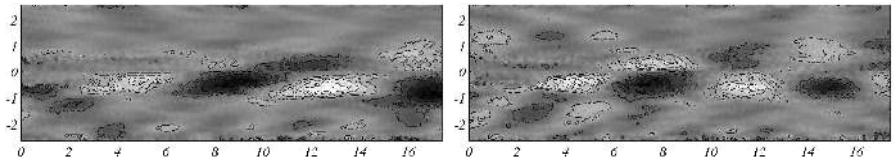

(c) $St = 0.06$ (d) $St = 0.07$

FIGURE 18. The streamwise component of four Koopman modes is shown. The associated Strohual number is reported in each label.

References

Álamo, J. C. D. & Jiménez, J. 2009 Estimation of turbulent convection velocities and corrections to taylor's approximation. *J. Fluid Mech.* **640**, 5.

Arnoldi, W. E. 1951 The principle of minimized iterations in the solution of the matrix eigenvalue problem. *Quart. Appl. Math.* **9**, 17–29.

Aubry, N. 1991 On the hidden beauty of the Proper Orthogonal Decompositon. *Theoret. Comput. Fluid Dyn.* **2**, 339–352.

Bagheri, S. 2010 Analysis and control of transitional shear layers using global modes. PhD thesis, KTH Mechanics, Sweden.

Bagheri, S., Hœpffner, J., Schmid, P. J. & Henningson, D. S. 2009 Input-output analysis and control design applied to a linear model of spatially developing flows. *Appl. Mech. Rev.* **62** (2).

Chua, L. & Lua, A. 1998 Measurements of a confined jet. *Physics of fluids* **10**, 3137.

Davidson, M. 2001 Self-sustained oscillation of a submerged jet in a thin rectangular cavity. *Journal of Fluids and Structures* .

Goldschmidt, V. & Bradshaw, P. 1973 Flapping of a plane jet. *Physics of Fluids* **16**, 354–355.

Holmes, P., Lumley, J. & Berkooz, G. 1996 *Turbulence Coherent Structures, Dynamical Systems and Symmetry*. Cambridge University Press.

Hussain, F. 1986 Coherent structures and turbulence. *J. Fluid Mech.* **173**, 303–356.

Ilak, M. & Rowley, C. W. 2008 Modeling of transitional channel flow using balanced proper orthogonal decomposition. *Phys. Fluids* **20**, 034103.

Loève, M. 1978 *Probability theory II*, 4th edn., , vol. Graduate Texts in Mathematics. Springer Verlag.

Lumley, J. L. 1970 *Stochastic Tools in Turbulence*. Academic Press, New York.

Maurel, A., Ern, P., Zielinska, B. & Wesfreid, J. 1996 Experimental study of self-sustained oscillations in a confined jet. *Physical Review E* **54** (4), 3643–3651.

Mezić, I. 2005 Spectral properties of dynamical systems, model reduction and decompositions. *Nonlinear Dynamics* **41** (1), 309–325.

Noack, B., Schlegel, B., Ahlborn, B., Mutschke, G., Norzynski, M., Comte, P. & Tadmor, G. 2008 A finite-time thermodynamics formalism for unsteady flows. *J. Non-Equilib. Thermodyn.* **33**, 103–148.

Örlu, R., Segalini, A., Alfredsson, P. & Talamelli, A. 2008 On the passive

control of the near-field of coaxial jets by means of vortex shedding. *Int. Conf. on Jets, Wakes and Separated Flows, ICJWSF-2008 September 16–19, 2008, Technical University of Berlin, Berlin, Germany* .

Rempfer, D. & Fasel, H. 1994 Evolution of three-dimensional coheren structures in a flat-plate boundary layer. *J. Fluid. Mech.* **260**, 351–375.

Rowley, C. W., Mezic, I., Bagheri, S., Schlatter, P. & Henningson, D. S. 2009 Spectral analysis of nonlinear flows. *J. Fluid Mech.* **641**, 115–127.

Ruhe, A. 1984 Rational Krylov sequence methods for eigenvalue computation. *Lin. Alg. Appl.* **58**, 391 – 405.

Saad, Y. 1980 Variations on Arnoldi's method for computing eigenelements of large unsymmetric matrices. *Lin. Alg. Appl.* **34**, 269–295.

Schmid, P., Violato, D. & Scarano, F. 2010 Analysis of time-resolved tomographic PIV data of a transitional jet. *Bulletin of the American Physical Society* .

Schmid, P. J. 2010 Dynamic Mode Decomposition. *J. Fluid Mech.* **656**, 5–28.

Sirovich, L. 1987 Turbulence and the dynamics of coherent structures i-iii. *Quart. Appl. Math.* **45**, 561–590.

Stanislas, M., Okamoto, K., Kähler, C. & Westerweel, J. 2008 Main results of the third international PIV challenge. *Experiments in Fluids* **45**, 27–71.

Willert, C. 2006 Assessment of camera models for use in planar velocimetry calibration. *Experiments in Fluids* **41**, 135–143.